TESS Asteroseismology of α Mensae: Benchmark Ages for a G7 Dwarf and Its M Dwarf Companion

Ashley Chontos[1,26] , Daniel Huber[1] , Travis A. Berger[1] , Hans Kjeldsen[2,3], Aldo M. Serenelli[4,5] , Victor Silva Aguirre[2] , Warrick H. Ball[2,6] , Sarbani Basu[7] , Timothy R. Bedding[2,8] , William J. Chaplin[2,6] , Zachary R. Claytor[1] , Enrico Corsaro[9] , Rafael A. Garcia[10,11] , Steve B. Howell[12] , Mia S. Lundkvist[2] , Savita Mathur[13,14] , Travis S. Metcalfe[15,16] , Martin B. Nielsen[2,6,17] , Jia Mian Joel Ong[7] , Zeynep Çelik Orhan[18] , Sibel Örtel[18] , Maissa Salama[19] , Keivan G. Stassun[20] , R. H. D. Townsend[21,22] , Jennifer L. van Saders[1] , Mark Winther[2] , Mutlu Yildiz[18] , R. Paul Butler[23] , C. G. Tinney[24] , and Robert A. Wittenmyer[25]

[1] Institute for Astronomy, University of Hawai'i, 2680 Woodlawn Drive, Honolulu, HI 96822, USA; achontos@hawaii.edu
[2] Stellar Astrophysics Centre (SAC), Department of Physics and Astronomy, Aarhus University, Ny Munkegade 120, DK-8000 Aarhus C, Denmark
[3] Institute of Theoretical Physics and Astronomy, Vilnius University, Sauletekio av. 3, 10257 Vilnius, Lithuania
[4] Institute of Space Sciences (ICE, CSIC) Campus UAB, Carrer de Can Magrans, s/n, E-08193, Barcelona, Spain
[5] Institut d'Estudis Espacials de Catalunya (IEEC), C/Gran Capita, 2-4, E-08034, Barcelona, Spain
[6] School of Physics and Astronomy, University of Birmingham, Edgbaston, Birmingham, B15 2TT, UK
[7] Department of Astronomy, Yale University, P.O. Box 208101, New Haven, CT 06520-8101, USA
[8] Sydney Institute for Astronomy (SIfA), School of Physics, University of Sydney, NSW 2006, Australia
[9] INAF—Osservatorio Astrofisico di Catania, via S. Sofia 78, I-95123, Catania, Italy
[10] IRFU, CEA, Université Paris-Saclay, F-91191 Gif-sur-Yvette, France
[11] AIM, CEA, CNRS, Université Paris-Saclay, Université Paris Diderot, Sorbonne Paris Cité, F-91191 Gif-sur-Yvette, France
[12] NASA Ames Research Center, Moffett Field, CA, 94035, USA
[13] Intituto de Astrofísica de Canarias (IAC), E-38205 La Laguna, Tenerife, Spain
[14] Universidad de La Laguna (ULL), Departmento de Astrofísica, E-38206 La Laguna, Tenerife, Spain
[15] Space Science Institute, 4765 Walnut Street, Suite B, Boulder, CO 80301, USA
[16] White Dwarf Research Corporation, 3265 Foundry Place, Unit 101, Boulder, CO 80301, USA
[17] Center for Space Science, NYUAD Institute, New York University Abu Dhabi, P.O. Box 129188, Abu Dhabi, United Arab Emirates
[18] Department of Astronomy and Space Sciences, Science Faculty, Ege University, 35100, Bornova, İzmir, Turkey
[19] Institute for Astronomy, University of Hawai'i, 640 North Aohoku Place #209, Hilo, HI 96720, USA
[20] Vanderbilt University, Department of Physics & Astronomy, 6301 Stevenson Center Lane, Nashville, TN 37235, USA
[21] Department of Astronomy, University of Wisconsin–Madison, 2535 Sterling Hall, 475 North Charter Street, Madison, WI 53706, USA
[22] Kavli Institute for Theoretical Physics, University of California, Santa Barbara, CA 93106, USA
[23] Earth & Planets Laboratory, Carnegie Institution for Science, 5241 Broad Branch Road NW, Washington, DC 20015, USA
[24] Exoplanetary Science at UNSW, School of Physics, UNSW Sydney, NSW 2052, Australia
[25] Centre for Astrophysics, University of Southern Queensland, USQ Toowoomba, QLD 4350, Australia

Abstract

Asteroseismology of bright stars has become increasingly important as a method to determine the fundamental properties (in particular ages) of stars. The Kepler Space Telescope initiated a revolution by detecting oscillations in more than 500 main-sequence and subgiant stars. However, most Kepler stars are faint and therefore have limited constraints from independent methods such as long-baseline interferometry. Here we present the discovery of solar-like oscillations in α Men A, a naked-eye ($V = 5.1$) G7 dwarf in TESS's southern continuous viewing zone. Using a combination of astrometry, spectroscopy, and asteroseismology, we precisely characterize the solar analog α Men A ($T_{eff} = 5569 \pm 62$ K, $R_\star = 0.960 \pm 0.016$ $R_\odot$, $M_\star = 0.964 \pm 0.045$ $M_\odot$). To characterize the fully convective M dwarf companion, we derive empirical relations to estimate mass, radius, and temperature given the absolute Gaia magnitude and metallicity, yielding $M_\star = 0.169 \pm 0.006$ $M_\odot$, $R_\star = 0.19 \pm 0.01$ $R_\odot$, and $T_{eff} = 3054 \pm 44$ K. Our asteroseismic age of 6.2 ± 1.4 (stat) ± 0.6 (sys) Gyr for the primary places α Men B within a small population of M dwarfs with precisely measured ages. We combined multiple ground-based spectroscopy surveys to reveal an activity cycle of $P = 13.1 \pm 1.1$ yr for α Men A, a period similar to that observed in the Sun. We used different gyrochronology models with the asteroseismic age to estimate a rotation period of ∼30 days for the primary. Alpha Men A is now the closest ($d = 10$ pc) solar analog with a precise asteroseismic age from space-based photometry, making it a prime target for next-generation direct-imaging missions searching for true Earth analogs.

1. Introduction

Accurate ages are essential for stellar astrophysics but arguably the most difficult fundamental property to determine.

Galactic archeology uses stellar ages to reconstruct the formation history of the Milky Way, while ages of exoplanet host stars are important to explain the diverse population of exoplanets observed today. Furthermore, ages will be important for next-generation space-based missions looking to image Earth-like planets orbiting Sun-like stars. For example, future

---
[26] NSF Graduate Research Fellow.

imaging missions would greatly benefit from an age-based target selection when attempting to identify biosignatures in the context of exoplanet habitability (Bixel & Apai 2020).

There are many techniques to estimate stellar ages but no single method suitable for all spectral types (Soderblom 2010). The most widely used is isochrone fitting, which is most fruitful for stellar clusters, where the main-sequence turnoff provides an age for an ensemble of stars. Isochrones also typically produce reliable ages for massive stars ($\gtrsim 1.5\,M_\odot$) or stars on the subgiant branch, for which stellar evolution is relatively quick. However, determining the ages of field stars is difficult, particularly for low-mass dwarfs that spend most of their lifetime on the main sequence. Consequently, many studies have focused on finding empirical relations between physically motivated age indicators and other observables in lower main-sequence stars.

Early disk-integrated Ca II H and K fluxes of the Sun revealed variations that correlated with the activity cycle, leading to one of the first empirical age relations. Activity in the Sun is generated through the magnetic dynamo mechanism, whose efficiency depends on subsurface convection and differential rotation (Kraft 1967). Pioneering work by Wilson (1978) observed these two chromospheric emission lines for nearly 100 cool main-sequence stars and demonstrated that many stars have cyclic variations analogous to that found in the Sun. In addition, studies of open clusters revealed an inverse relationship between stellar age and activity (Wilson 1963, 1966; Skumanich 1972; Soderblom et al. 1991). An empirical relation between chromospheric activity and age was established and would ultimately be the leading age indicator for later-type field stars for decades (Noyes et al. 1984; Baliunas et al. 1995; Henry et al. 1996; Wright et al. 2004).

Another empirical relation uses stellar rotation periods to estimate ages based on the spin-down of stars with time (gyrochronology). This mechanism is enabled by magnetic braking, where charged particles escape through magnetized winds, leading to mass and angular momentum loss (Skumanich 1972). Factoring in a mass (or color) dependence, Barnes (2007) derived an empirical rotation–age relation that successfully reproduced the ages of young clusters to better than 20%. Gyrochronology recently underwent a resurgence with Kepler (Borucki et al. 2010) through the measurement of rotation periods for more than 30,000 main-sequence stars (Nielsen et al. 2013; Reinhold et al. 2013; McQuillan et al. 2014; Santos et al. 2019).

The success of empirical age relations makes it critical to verify them with independent calibrations. Recently, gyrochronology relations have failed to reproduce rotation rates for intermediate-age clusters from K2, suggesting that the standard formalism needs to be adjusted (Curtis et al. 2019; Douglas et al. 2019). Moreover, van Saders et al. (2016) proposed a weakened braking law to explain the unexpected rapid rotation in older stars, indicating an additional source of uncertainty for rotation-based ages. This is further complicated for low-mass dwarfs that barely evolve over the nuclear timescale and hence are also challenging to age through isochrones. Therefore, ages for lower main-sequence stars remain challenging and limited, which is largely due to the lack of calibrators in this regime.

A powerful method to determine accurate ages of field stars is asteroseismology, especially for solar-like oscillations driven by near-surface convection. Kepler revolutionized the field but only detected oscillations in ~500 main-sequence and subgiant stars, most of which are quite faint (Chaplin et al. 2014;

García & Ballot 2019). The Transiting Exoplanet Survey Satellite (TESS; Ricker et al. 2015) is now targeting much brighter stars (e.g., Chaplin et al. 2020) for which we also have long-term activity monitoring, enabling the opportunity to add benchmark calibrators for alternative age determination methods.

Here we present the TESS discovery of solar-like oscillations in alpha Mensae, which is now the closest solar analog with an asteroseismic detection from space. Alpha Men A is a naked-eye G7 star ($V = 5.1$) in TESS's southern continuous viewing zone (SCVZ). It has an M dwarf companion that we can now age-date using asteroseismology of the primary, making it an ideal target to age-date two lower main-sequence stars and providing an invaluable nearby benchmark system.

2. Observations

2.1. TESS Photometry

Alpha Mensae falls in the TESS SCVZ and thus was observed for the entire first year of the nominal mission. Alpha Men was observed in a 2 minute cadence for all 13 sectors, for a total baseline of 351 days. We used the light-curve files produced by the TESS Science Processing Operations Center (SPOC; Jenkins et al. 2016) that were made publicly available on the Mikulski Archive for Space Telescopes (MAST).[27]

We downloaded all SPOC 2 minute light curves and stitched individual sectors together using the SPOC-processed Pre-data Conditioning Standard Aperture Photometry (PDCSAP) flux. Upon initial inspection of the light curve (Figure 1), we noticed two sectors with increased scatter by a factor of at least 2. We suspected that this was due to instrumental systematics and therefore removed these data before further analysis. To prepare the light curve for asteroseismic analysis, bad data points were removed as described in Chontos et al. (2019), including points with poor quality flags, $>5\sigma$ outliers, or sharp time-domain artifacts, which ultimately accounted for ~25% of the data.

2.2. High-resolution Spectroscopy

Alpha Mensae is a well-studied star, with 28 different sets of spectroscopic parameters available on Simbad.[28] Retaining only results from 1980 onward that used high-resolution instruments, a total of 14 independent spectroscopic parameters remained and are listed in Table 1. We adopted the values from Ramírez et al. (2012) and then added the standard deviation of the literature values in quadrature with the reported formal uncertainties. The final set of atmospheric parameters for α Men A is $T_{\rm eff} = 5569 \pm 50$ (stat) ± 36 (sys) K, $\log g = 4.42 \pm 0.03$ (stat) ± 0.06 (sys) dex, and $[{\rm Fe/H}] = 0.11 \pm 0.05$ (stat) ± 0.03 (sys) dex (Table 2). We also checked the alpha abundances (in particular [Mg/Fe] and [Ca/Fe]) and found them to be consistent with solar values (Bensby et al. 2014).

2.3. Broadband Photometry and Gaia Parallax

Due to its brightness ($V = 5.1$), α Men A is saturated in many large photometric surveys. For optical magnitudes, we relied on B_T and V_T magnitudes from the Tycho-2 catalog (Høg et al. 2000). Cutri et al. (2012) reported reliable quality flags for J, H, and K_S photometry in the extended Two Micron All Sky
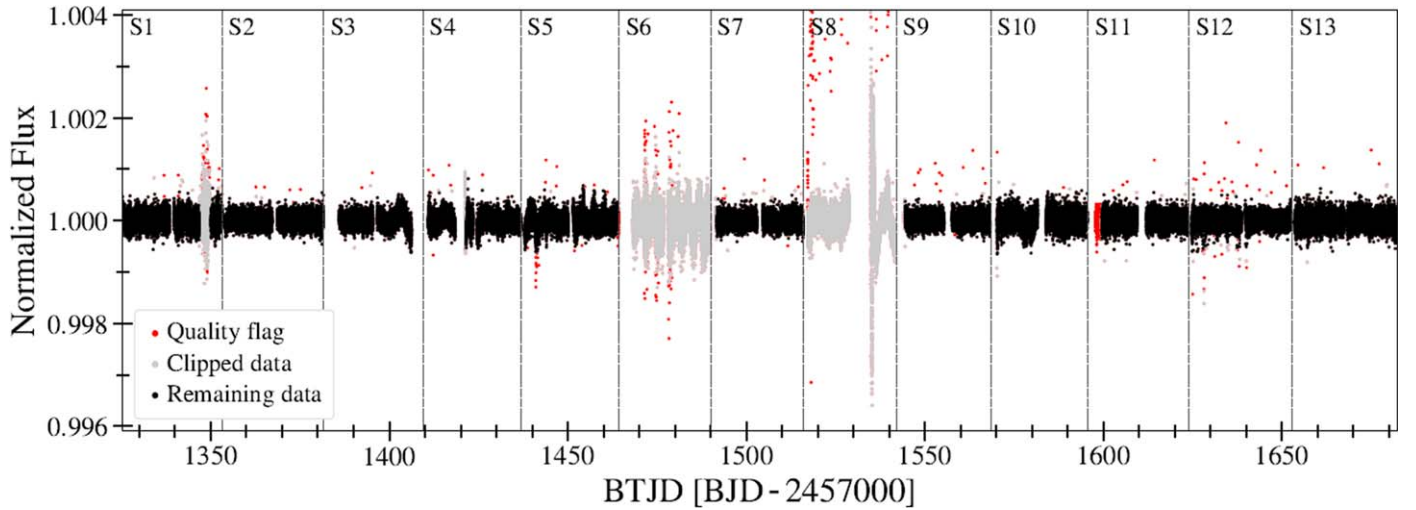
----

[27] https://mast.stsci.edu/portal/Mashup/Clients/Mast/Portal.html
[28] http://simbad.u-strasbg.fr/simbad/

Figure 1. Normalized TESS light curve of α Mensae A. Red points were removed based on quality flag information, gray points were clipped according to Chontos et al. (2019), and the remaining black points ($\sim$75% of the original data) were used in the asteroseismic analysis. Dashed lines delineate the 13 sectors.

Table 1
Literature Sources for Spectroscopic T_{eff}, $\log g$, and [Fe/H] Values Discussed in Section 2.2

Source	T_{eff} [K]	$\log g$ [cgs]	[Fe/H]
Santos et al. (2001)	5620	4.56	0.12
Bensby et al. (2003)	5550	4.38	0.10
Santos et al. (2004)	5594	4.41	0.10
Valenti & Fischer (2005)	5587	4.50	0.09
Bond et al. (2006)	5557	4.43	0.06
Ramírez et al. (2007)	5536	4.50	0.12
Bruntt et al. (2010)	5570	4.43	0.15
Casagrande et al. (2011)	5605		
da Silva et al. (2012)	5630	4.47	0.11
Maldonado et al. (2012)	5649	4.60	0.12
Ramírez et al. (2012)	5569	4.42	0.11
Bensby et al. (2014)	5517	4.48	0.07
Maldonado et al. (2015)	5607	4.51	
Luck (2018)	5589	4.44	0.15

Table 2
Primary Stellar Parameters

Other Identifiers:		
α Men, HR 2261, HD 43834,		
HIP 29271, Gaia DR2 5264749303461634816,		
Gaia eDR3 5264749303462961280, TIC 141810080		

Parameter	Value	Source
R.A., α_{J2016}	92.5624	1, 2
decl., δ_{J2016}	-74.7540	1, 2
Parallax, π (mas)	97.9158 ± 0.0573	1, 2
Distance, d (pc)	10.2129 ± 0.0060	1, 2
Spectral type	G7V	3
Photometry		
Tycho-2 B mag, B_T	5.968 ± 0.014	4
Tycho-2 V mag, V_T	5.151 ± 0.009	4
2MASS J mag, J	3.951 ± 0.232	5, 6
2MASS H mag, H	3.508 ± 0.228	5, 6
2MASS K_S mag, K_S	3.446 ± 0.200	5, 6
Gaia G mag, G[a]	4.8973 ± 0.0025	1, 2
Gaia Bp mag, Bp	5.2783 ± 0.0024	1, 2
Gaia Rp mag, Rp	4.3900 ± 0.0023	1, 2
Spectroscopy and Gaia		
Effective temperature, T_{eff} (K)	$5569 \pm 50(36)$	7
Metallicity, [Fe/H] (dex)	$0.11 \pm 0.05(0.03)$	7
Surface gravity, $\log g$ (cgs)	$4.42 \pm 0.03(0.06)$	7
Projected rotation speed, $v \sin i$ (km s^{-1})	0.6 ± 0.6	8
Luminosity, $L_\star$ ($L_\odot$)	0.81 ± 0.02	
Asteroseismology		
Stellar mass, $M_\star$ ($M_\odot$)	$0.964 \pm 0.037(0.026)$	
Stellar radius, $R_\star$ ($R_\odot$)	$0.960 \pm 0.013(0.009)$	
Stellar density, $\rho_\star$ (gcc)	$1.531 \pm 0.018(0.011)$	
Surface gravity, $\log g$ (cgs)	$4.459 \pm 0.006(0.004)$	
Age, t (Gyr)	$6.2 \pm 1.4(0.6)$	

Note.
[a] Magnitude has been corrected for saturation according to Evans et al. (2018).
References–(1) Gaia Collaboration et al. (2016); (2) Gaia Collaboration et al. (2021); (3) Gray et al. (2006); (4) Høg et al. (2000); (5) Cutri et al. (2003); (6) Skrutskie et al. (2006); (7) Ramírez et al. (2012); (8) Bruntt et al. (2010).

Survey (2MASS) catalog, although we note the higher uncertainties due to the choice of aperture needed for saturated stars. The European Space Agency's (ESA) Gaia Data Release 2 (DR2;[29] Gaia Collaboration et al. 2018) estimated a mean Gaia magnitude $G = 4.850$ for α Men. Brighter sources in DR2 photometry ($G < 6$) suffer from systematic errors due to saturation (Evans et al. 2018). Using the empirical correction in Evans et al. (2018), we calculated a corrected Gaia magnitude, $G = 4.897$. The new early Gaia Data Release 3 (eDR3) catalog reported a value of $G = 4.900$ for the primary and is therefore consistent with the corrected magnitude used in this analysis (Gaia Collaboration et al. 2021; Riello et al. 2021).

Using the Tycho-2 B_T and V_T magnitudes, we derived two luminosities with `isoclassify`[30] (Huber 2017). The magnitude was combined with the Gaia parallax, bolometric corrections from MIST isochrones (Choi et al. 2016), and the composite reddening map `mwdust`[31] (Bovy et al. 2016), yielding $L_\star = 0.800 \pm 0.008 L_\odot$ (B_T) and $L_\star = 0.812 \pm 0.007 L_\odot$ (V_T).

As an independent check on the derived luminosity, we analyzed the broadband spectral energy distribution (SED) together with the Gaia DR2 parallax following the procedures described by Stassun et al. (2017, 2018). We took the near-UV flux from the Galaxy Evolution Explorer; the Johnson U, B, and V magnitudes from Mermilliod (2006); the Strömgren u, v, b, and y magnitudes from Paunzen (2015); the B_T and V_T magnitudes from Tycho-2; the J, H, and K_S magnitudes from 2MASS; the $W1$–$W4$ magnitudes from the Wide-field Infrared Survey Explorer; and the G, G_{BP}, and G_{RP} magnitudes from Gaia. Together, the available photometry spans a wavelength range of 0.2–22 μm.

We performed a fit using Kurucz stellar atmosphere models, adopting the effective temperature (T_{eff}), surface gravity ($\log g$), and metallicity ([Fe/H]) from the spectroscopically determined values. The extinction (A_V) was set to zero due to the star being very nearby. The resulting fit has a reduced χ^2 of 2.4. Integrating the (unreddened) model SED gives a bolometric flux at Earth of $F_{bol} = 2.494 \pm 0.058 \times 10^{-7}$ erg s^{-1} cm^{-2}. Taking F_{bol} and T_{eff} together with the Gaia parallax (adjusted by $+0.08$ mas to account for the systematic offset reported by Stassun & Torres 2018) gives a stellar radius $R_\star = 0.968 \pm 0.021\,R_\odot$ and bolometric luminosity $L_{bol} = 0.810 \pm 0.019\,L_\odot$. We performed an additional fit excluding the Gaia magnitudes to test if the known systematics affected the derived properties, but the results were unchanged. The derived values from the SED fit are in good agreement with those derived using isoclassify.

Similar to the method discussed in Section 2.2 for the spectroscopic parameters, we performed a literature search for Gaia- and Hipparcos-derived luminosities to account for systematic differences. We used bolometric luminosities from seven independent studies (Bruntt et al. 2010; Casagrande et al. 2011; Eiroa et al. 2013; Heller et al. 2017; McDonald et al. 2017; Stevens et al. 2017; Schofield et al. 2019) along with the three luminosities derived in our study to determine the scatter in the values. We adopted the isoclassify result using the Tycho-2 V_T magnitude and added the standard deviation of the 10 values ($\sigma_{L_\star} = 0.018\,L_\odot$) in quadrature with our derived uncertainty ($\sigma_{L_\star} = 0.007\,L_\odot$), yielding a bolometric luminosity $L_\star = 0.81 \pm 0.02\,L_\odot$. The median value for the 10 luminosities was slightly higher at $L_\star = 0.828$ but is within 1σ of our final reported value.

3. Asteroseismology

3.1. Background Fit

A high-pass filter was applied to the TESS 2 minute light curve (Figure 1) to remove long-period trends. The power spectrum was then calculated using a Lomb–Scargle periodogram (Lomb 1976; Scargle 1982) through the publicly available astropy package. The power spectrum in Figure 2(a) shows a flat white-noise component and a correlated red-noise signal that rises at lower frequencies, indicative of stellar granulation. A roughly Gaussian power excess due to oscillations is clearly visible at $\sim 3200\ \mu$Hz (Figure 2(b)).

A common approach to model the power spectra of solar-like oscillators typically has the form

$$f(\nu) = W + R(\nu)[B(\nu) + G(\nu)], \qquad (1)$$

where $f(\nu)$ is the power density at frequency ν (Mathur et al. 2011; Corsaro et al. 2018). The frequency-independent term

(W) is due to photon noise. The response function, $R(\nu)$, is an attenuation factor that affects the observed spectral amplitudes due to the sampling rate (or cadence) in a time series. The attenuation is greater for oscillations that occur near the Nyquist frequency, which for TESS 2 minute data is $\nu_{Nyq} = 4166.67\ \mu$Hz. The last two terms in Equation (1) refer to contributions from the stellar granulation background $B(\nu)$ and the Gaussian envelope of oscillations $G(\nu)$.

To determine the stellar background contribution, we used the publicly available Background,[32] which is a software extension of DIAMONDS.[33] Initially created for more robust asteroseismic analyses, DIAMONDS is a nested sampling Monte Carlo (NSMC) algorithm for Bayesian parameter estimation and model comparison (Corsaro & De Ridder 2014). The background model built into this framework has the functional form

$$B(\nu) = \zeta \sum_{i=1}^{n} \frac{\sigma_i^2/\nu_i}{1 + (\nu/\nu_i)^4}, \qquad (2)$$

where ζ is a normalization factor ($2\sqrt{2}/\pi$), σ_i is the amplitude, and ν_i is the characteristic frequency for n Harvey-like components (Harvey 1985). Different stellar background contributions like granulation and mesogranulation have typical characteristic frequencies of $\sim\nu_{max}$ and $\sim\nu_{max}/3$ for solar-like oscillators (Corsaro et al. 2017).

We used the following configuration for the NSMC analysis: shrinking rate, $\alpha = 0.02$; enlargement fraction, $f_0 = 1.43$; number of live points, $N_{live} = 500$; number of clusters, $3 \leqslant N_{clust} \leqslant 6$; maximum attempts when drawing a new sampling point, $M_{attempts} = 5 \times 10^4$; initial number of live points, $M_{init} = N_{live}$; and clustering only happens every N iterations or $M_{same} = 50$. Aside from minor changes to the shrinking rate (α) and enlargement fraction (f_0), which control the sampling efficiency based on the number of free parameters in the model, the other parameters were the same as what was provided in the DIAMONDS documentation. We refer the reader to Corsaro & De Ridder (2014) for more details about the software.

Ultimately, the data did not provide enough evidence for DIAMONDS to converge on reliable results for more complex models (i.e., multiple Harvey-like terms), and therefore no model comparison was needed. We attempted to model the granulation component, but it was mostly unconstrained or resulted in very small amplitudes. This is likely because the amplitude of the granulation signal is comparable to or less than the white-noise level in the power spectrum. The final background fit is shown in Figure 2(a) as a solid blue line, which is the summed contributions from a white-noise component (dashed blue line) and a mesogranulation term (dotted blue line).

3.2. Global Asteroseismic Parameters

The shaded region in Figure 2(b) shows the power excess due to oscillations. Within the DIAMONDS framework, this power excess is modeled by a Gaussian,

$$G(\nu) = H_{osc} \exp\left[-\frac{(\nu - \nu_{max})^2}{2\sigma_{osc}^2}\right], \qquad (3)$$
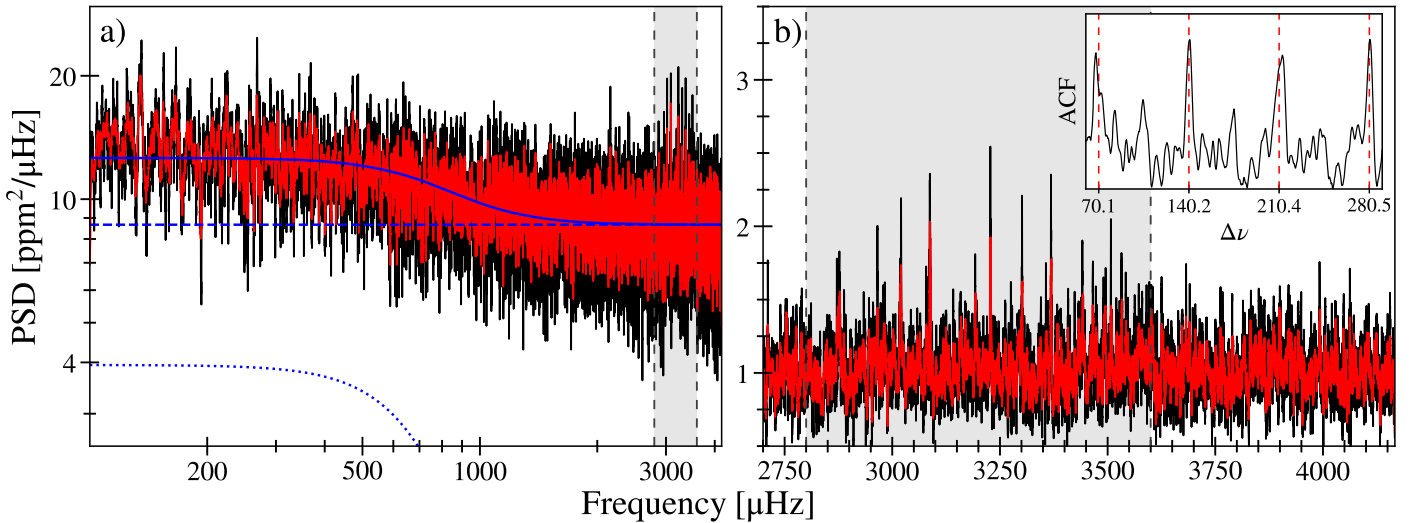
Figure 2. Panel (a): power spectrum of α Men A using box filters of 1.0 and 2.5 μHz shown in black and red, respectively. The total background fit from DIAMONDS due to stellar contribution is shown by a solid blue line, which is the combination of a mesogranulation component (dotted blue line) and a white-noise component (dashed blue line). Panel (b): background-corrected power spectrum centered on the power excess due to stellar oscillations, highlighted in the shaded region. The power in this region is used to calculate an autocorrelation, shown in the inset. Dashed lines in the inset represent expected peaks in the autocorrelation due to the characteristic spacings of p-mode oscillations.

centered at ν_{max} with height H_{osc} and width σ_{osc} (Corsaro & De Ridder 2014). The resulting parameters of the global DIAMONDS analysis for α Men A are listed in Table 3.

We also derived an independent value for the frequency corresponding to maximum power using the SYD pipeline (Huber et al. 2009), yielding $\nu_{max} \sim 3267$ μHz, consistent with the results from DIAMONDS. Two independent analyses additionally confirmed a power excess in the same region, with $\nu_{max} = 3230$ μHz (A2Z; Mathur et al. 2010) and $\nu_{max} = 3216$ μHz (Lundkvist et al. 2014), both consistent to $\lesssim 1\sigma$ from our derived values. Our derived ν_{max} is larger than that in the Sun ($\nu_{max,\odot} = 3090$ μHz). Therefore, α Men A joins only a handful of other stars, such as τ Cet (Teixeira et al. 2009), α Cen B (Carrier & Bourban 2003; Kjeldsen et al. 2005), and Kepler-444 (Campante et al. 2015), that have a higher ν_{max} than the Sun.

To estimate a preliminary value for the large frequency separation, we calculated an echelle diagram. In the case of solar-like oscillators, modes of different radial order (n) with the same spherical degree (ℓ) should form vertical ridges if the correct spacing is used. We calculated the best-fitting value by taking small steps in frequency space until the ridges lined up vertically, yielding $\Delta\nu \sim 140$ μHz. Figure 4 shows the resulting echelle diagram created using echelle[34] (Hey & Ball 2020), which clearly confirms the detection of solar-like oscillations.

3.3. Individual Frequencies

We extracted frequencies from the background-corrected power spectrum using three independent methods, which are based on fitting Lorentzian profiles to individual modes (García et al. 2001, 2009; Handberg & Campante 2011; Nielsen et al. 2015, 2017). A second approach used an alternative power spectrum calculated using weights to account for different noise levels across time series (Arentoft et al. 2008).

Table 3
DIAMONDS Background Fit Using $n = 1$ Harvey-like Component

Parameter	Value
White noise, W	8.67 ± 0.05 ppm^2 μHz^{-1}
Mesogranulation timescale, τ_{meso}	20.6 ± 0.8 minutes
Mesogranulation amplitude, σ_{meso}	59.5 ± 1.1 ppm
Gaussian height, H_{osc}	0.145 ± 0.129 ppm^2 μHz^{-1}
Gaussian center, ν_{max}	3134.28 ± 439.91 μHz
Gaussian width, σ_{osc}	403 ± 279 μHz

Note. Values are calculated by taking the median $\pm 1\sigma$ (credible level of 68.3%) from each parameter posterior distribution.

To compare the two approaches, Figure 4 shows both the unweighted (solid gray regions, original; black lines, smoothed) and weighted (dotted black lines) power spectra stacked by radial order n about ν_{max}. The figure clearly exhibits the consistency between the two independently calculated spectra, especially for the higher signal-to-noise ratio modes.

Our final frequency list was constructed by taking modes for which both approaches reported a detection. We report four radial ($\ell = 0$), four dipole ($\ell = 1$), and two quadrupole ($\ell = 2$) modes in Table 4. Formal uncertainties were adopted using the frequencies calculated from the weighted power spectrum and adding in quadrature the scatter in frequencies derived from independent methods to account for systemic uncertainties. The final set of frequencies are plotted on the echelle diagram (Figure 3, marked by their spherical degree ℓ) and the stacked power spectrum (Figure 4).

3.4. Frequency Modeling

To properly account for systematic uncertainties, we derived the fundamental stellar properties of α Men A using nine independent modeling pipelines, including BASTA (Silva Aguirre et al. 2015), YB (Basu et al. 2010; Gai et al. 2011; Basu et al. 2012), AMP[35] (Metcalfe & Charbonneau 2003;
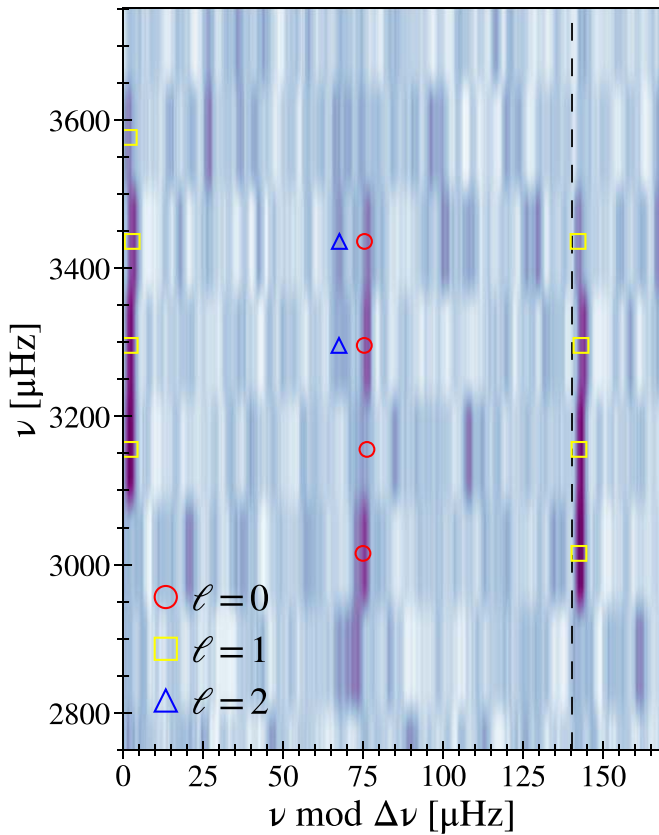
---

[34] https://github.com/danhey/echelle

[35] https://github.com/travismetcalfe/amp2

Figure 3. Echelle diagram of α Men A from a smoothed power spectrum (with a boxcar filter width of 2.5 μHz) using echelle (Hey & Ball 2020). Different oscillation modes are marked and colored by their spherical degree: radial modes ($\ell = 0$) with red circles, dipole modes ($\ell = 1$) with yellow squares, and quadrupole modes ($\ell = 2$) with blue triangles. The large frequency separation derived from radial modes is $\Delta\nu = 140.24 \pm 1.98$ μHz and delineated by the black dashed line.

Table 4
Extracted Mode Identifications and Oscillation Frequencies for α Men A Sorted by Spherical Degree ℓ

ν (μHz)	σ_ν (μHz)	n	ℓ
3019.95	0.50	23	0
3161.43	0.99	24	0
3300.84	0.69	25	0
3441.14	0.87	26	0
3087.44	0.59	23	1
3227.69	0.52	24	1
3368.55	0.44	25	1
3507.88	0.58	26	1
3292.93	0.47	24	2
3433.30	0.95	25	2

Metcalfe et al. 2009a, 2012a), BeSPP (Serenelli et al. 2013, 2017), Izmir (Yıldız et al. 2019), GOE (Silva Aguirre et al. 2017), and YALE-M (Mier 2017; Ball et al. 2020). Model grids were calculated from various stellar evolution codes (YY, Demarque et al. 2004; MESA r10398, r12115, r15140, Paxton et al. 2011, 2013, 2015, 2018, 2019; GARSTEC, Weiss & Schlattl 2008; YREC, Demarque et al. 2008; BaSTI, Pietrinferni et al. 2004; DSEP, Dotter et al. 2007, 2008; CESAM2k, Morel & Lebreton 2008; YREC2, Basu et al. 2012; ASTEC, Christensen-Dalsgaard 2008; CESTAM, Girardi et al.

2000; Marigo et al. 2008; Marques et al. 2013; and Padova) using different assumptions about input physics. Oscillation frequencies were generated from oscillation codes (ADIPLS, Christensen-Dalsgaard 2008; GYRE, Townsend & Teitler 2013), where most of the methods listed here also applied corrections for near-surface effects (Kjeldsen et al. 2008; Ball & Gizon 2014).

Each method derived four sets of stellar parameters based on the following sets of constraints.

1. { $T_{\rm eff}$, [Fe/H], $L_\star$, $\nu_{\rm max}$, $\Delta\nu$, $\nu(n, 0)$, $\nu(n, 1)$, $\nu(n, 2)$}.
2. { $T_{\rm eff}$, [Fe/H], $\nu_{\rm max}$, $\Delta\nu$, $\nu(n, 0)$, $\nu(n, 1)$, $\nu(n, 2)$}.
3. { $T_{\rm eff}$, [Fe/H], $L_\star$, $\nu_{\rm max}$, $\Delta\nu$, $\nu(n, 0)$, $\nu(n, 1)$}.
4. { $T_{\rm eff}$, [Fe/H], $\nu_{\rm max}$, $\Delta\nu$, $\nu(n, 0)$, $\nu(n, 1)$}.

The main purpose for all four runs was to test for inconsistencies between the luminosity derived from aster-oseismology and the independent Gaia-derived luminosity, as well as to check if the weaker quadrupole ($\ell = 2$) modes had any affect on the final age estimates. Results from each pipeline were self-consistent in that the runs that excluded the quadrupole modes generally preferred younger ages, but ultimately, the differences were not significant ($\leqslant 10\%$) and $\lesssim 1\sigma$. Moreover, across the numerous methods and model inputs mentioned, the derived stellar parameters between all pipelines agreed to within 1σ.

For the final stellar parameters, we adopted the results from the Bellaterra Stellar Properties Pipeline (BeSPP; Serenelli et al. 2013, 2017), which was closest to the median values for the fundamental stellar parameters (mass and age) in case 1. BeSPP constructed a grid of stellar models with GARSTEC (Weiss & Schlattl 2008) using a gray model atmosphere based on Vernazza et al. (1981), the solar mixture model from Grevesse & Noels (1993), and the diffusion of elements according to Thoul et al. (1994). We refer the reader to Weiss & Schlattl (2008) for more details on the input physics of stellar models computed with GARSTEC. BeSPP yielded a bimodal solution as a result of a bimodal surface correction, which, at a fixed mass, was older (~ 2 Gyr) and more metal-rich (~ 0.1 dex). The surface correction for the younger solution was unexpectedly large (~ 50 μHz) for a solar analog and hence provided strong support in favor of the older model.

To account for systematic differences between various methods, uncertainties were calculated by adding the standard deviation for each parameter {M, R, ρ, τ, $\log g$} from all pipelines in quadrature with the formal uncertainty from BeSPP. Corrected model frequencies are plotted with the observed frequencies in an echelle diagram in Figure 5. Stellar parameters are listed in Table 2 (i.e., see the asteroseismology section), with fractional uncertainties of 1.4% (1.2% stat ± 0.7% sys) in density, 1.7% (1.4% stat ± 0.9% sys) in radius, 4.7% (3.9% stat ± 2.7% sys) in mass, and 24.2% (21.8% stat ± 10.4% sys) in age.

4. M Dwarf Companion

4.1. Discovery and Initial Characterization

A bound M dwarf companion to α Men A was first identified by Eggenberger et al. (2007) in a study investigating the impact of stellar duplicity on planet occurrence rates using adaptive optics imaging with NACO/VLT. Eggenberger et al. (2007) ruled out the possibility of HD 43834 B being a background star, stating that the astrometry was compatible with orbital
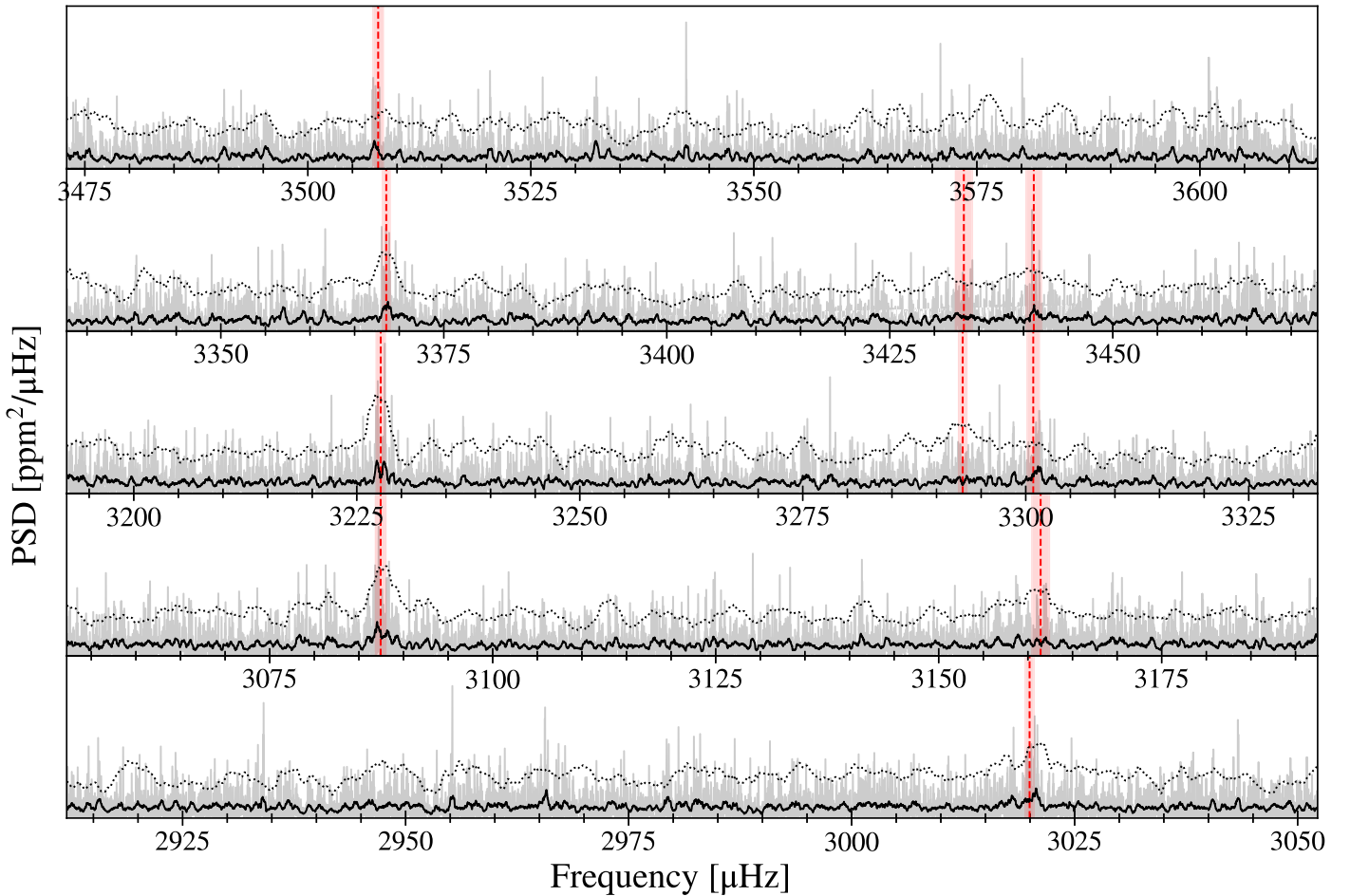
Figure 4. Power spectrum of α Men A arranged in echelle format. The original power spectrum calculated using TESS data (Section 2.1) is shown in gray, as well as a smoothed version of the same power spectrum (using a boxcar width = 1.5 μHz) in black. The weighted power spectrum discussed in Section 3.4 is overplotted with a dotted black line with a vertical offset for direct comparison. The final frequencies from Table 4 are added in red, where the shaded regions are equal to $\pm 1\sigma$ for each mode.

motion. In addition, they added that the physical association was further supported by a linear drift present in CORA-LIE data.

Eggenberger et al. (2007) reported a magnitude difference of $\Delta m = 4.97 \pm 0.05$ in the narrowband K filter ($\lambda_c = 2.166 \mu$m). After a correction to account for the differences in relative photometric systems, they reported an absolute 2MASS K_S magnitude, $M_{K_s} = 8.43 \pm 0.05$, for the companion. They concluded that HD 43834 B is consistent with an M3.5–M6.5 dwarf companion with a mass of $M_{\star,B} = 0.14 \pm 0.01\, M_\odot$ at a projected separation of 3″ from the primary, which corresponds to a physical separation of $\sim$30 au. Tokovinin (2014) characterized nearby multiple star systems and, using the literature mass of $M_{\star,A} = 1.01\, M_\odot$ for the primary, estimated an orbital period of $\sim$162 yr for the wide companion.

4.2. A Search for Additional Companions

To search for additional close companions, we observed α Mensae with Zorro,[36] a dual-channel imager on the 8.1 m telescope at the Gemini South Observatory (Cerro Pachon, Chile). Zorro provides simultaneous diffraction-limited optical imaging (FWHM 0″02 at 650 nm) in two channels. We

observed α Men A in speckle mode to search for close-in companions between UT 2019 December 22 and 2019 December 23. The images were subjected to the standard Fourier analysis as described in Howell et al. (2011) and used to produce reconstructed images in each color, providing high-resolution angular results. In addition to detecting the M dwarf companion at 3″ distance, no other companions to Mensae were found. Figure 6 shows the contrast curves from the reduced speckle data in both bands, indicating that there are no additional close companions ($<1″2$) from the diffraction limits down to contrasts of $\Delta m \sim 7$ in the r band (562 nm) and $\Delta m \sim 8$ in the z band (832 nm). At the distance of α Mensae, these angular limits correspond to spatial limits of 0.2–1.2 au.

4.3. Revised Properties of α Men B

The wide companion was resolved in Gaia DR2, which reported a magnitude of $G = 11.8057$ and a contrast of $\Delta G = 6.955$. However, eDR3 (Gaia Collaboration et al. 2021; Riello et al. 2021) reported a significantly fainter companion with $G = 12.365$, corresponding to a contrast of $\Delta G = 7.465$. Additionally, eDR3 provided a parallax for the companion, which was unavailable in DR2.

In order to estimate the companion properties, we derived empirical relations for masses, effective temperatures, and radii of M dwarfs given the absolute Gaia magnitude (M_G). We
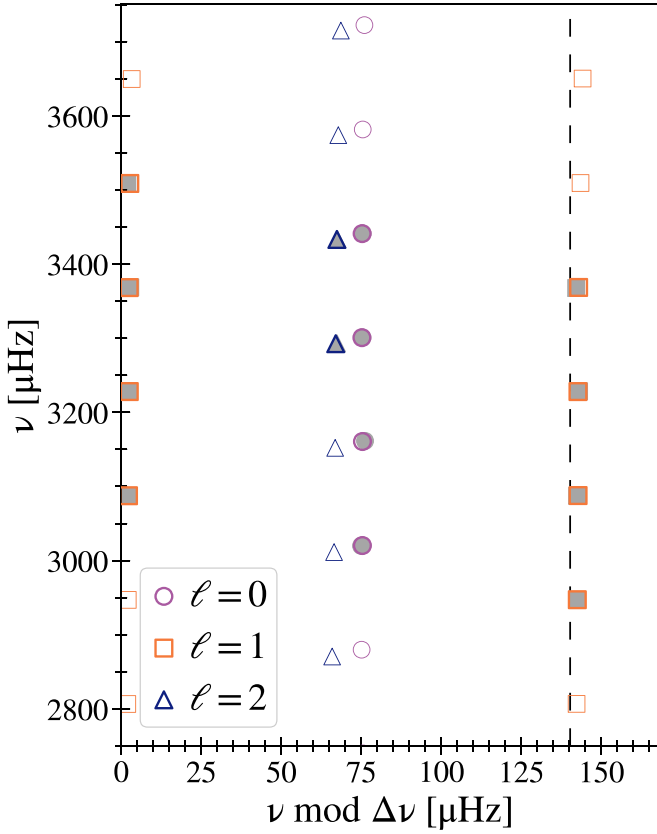
---

[36] https://www.gemini.edu/instrumentation/current-instruments/alopeke-zorro

Figure 5. Echelle diagram of observed frequencies (filled gray symbols) and best-fit model frequencies (open colored symbols) using `BeSPP` (Serenelli et al. 2013, 2017). Modeled frequencies that correspond to an observed frequency are highlighted with a thick outline.
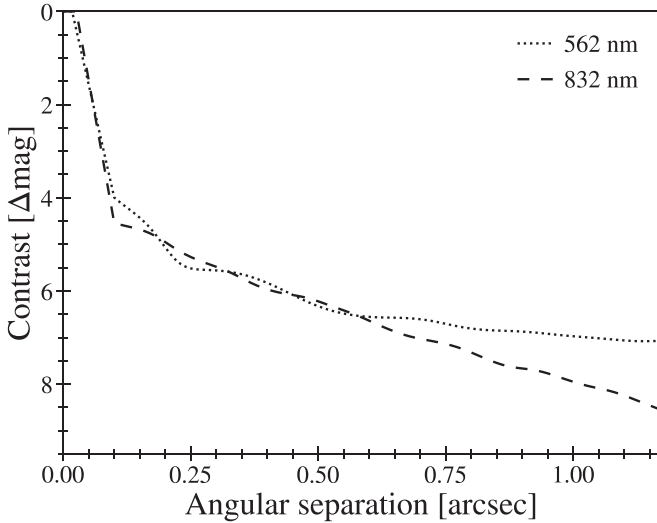

Figure 6. Detection limits from speckle imager Zorro on the Gemini South telescope in the r and z bands (562 and 832 nm, respectively), ruling out any additional close-in companions to the contrast levels obtained.

adopted the T_{eff} and radius values from Mann et al. (2015) and used the M_K–mass relation from Mann et al. (2019) to estimate the M dwarf masses. We computed the absolute Gaia magnitudes using eDR3 (Gaia Collaboration et al. 2021) photometry (Riello et al. 2021) and parallaxes (Lindegren et al. 2021), including the relevant corrections when applicable. We removed two stars from the Mann et al. (2015) sample for our

relations: Gl 896 B due to its largely discrepant measurements in mass, T_{eff}, and radius and FBS L 10–72 due to its discrepant [Fe/H] given its other measured values. For each of the three parameters (T_{eff}, $R_\star$, $M_\star$), we optimized polynomial coefficients using a least-squares minimization method available with `scipy`. Finally, to select the optimal order, we chose the curve that minimized the Bayesian information criterion (Schwarz 1978).

Figure 7 shows the resulting relations, which are

$$M_\star = -7.0653 + 3.0293x - 0.4218x^2$$
$$+ 0.0244x^3 - 0.0005x^4 + 0.1771y - 0.0087xy, \quad (4)$$

$$T_{eff} = 19938.4 - 4999.7x + 582.0x^2$$
$$- 30.8x^3 + 0.6x^4 - 131.0y + 208.0y^2, \quad (5)$$

and

$$R_\star = (-4.1305 + 1.9735x - 0.2832x^2$$
$$+ 0.0166x^3 - 0.0003x^4) \times (1 + 0.2450y), \quad (6)$$

where x is the absolute Gaia magnitude M_G from eDR3 and y is the metallicity from Mann et al. (2015).

Using the Gaia absolute magnitude for α Men B and metallicity for α Men A, the relations yield a mass of $M_\star = 0.169 \pm 0.006\ M_\odot$, radius of $R_\star = 0.19 \pm 0.01\ R_\odot$, and $T_{eff} = 3054 \pm 44$ K for α Men B. Uncertainties were calculated from the residual scatter between the models and data and are 3.7% in mass, 4.4% in radius, and 44 K in T_{eff}. The mass uncertainty was calculated using the scatter of 2.2% in our derived relation (Equation (4)) added in quadrature with the conservative estimate of 3% from the Mann et al. (2019) $M_{Ks} - M_\star$ relation. Notably, our derived mass of $0.169 \pm 0.006\ M_\odot$ for the fully convective M dwarf is slightly higher than the value of $0.14 \pm 0.01\ M_\odot$ from Eggenberger et al. (2007), which was based on an infrared mass–luminosity relation for low-mass stars. All observed and derived properties of α Men B are summarized in Table 5.

5. Discussion

5.1. Testing Stellar Physics with Asteroseismology

Asteroseismology of nearby bright stars allows us to test stellar models by combining with other high-resolution stellar classification techniques like spectroscopy, interferometry, and astrometry (Bruntt et al. 2010; Silva Aguirre et al. 2012; Hawkins et al. 2016). An example is Bruntt et al. (2010), who combined interferometry, asteroseismology, and spectroscopy to derive the most accurate and precise fundamental properties for 23 bright stars.

Figure 8 shows the radii and distances of stars in which solar-like oscillations have been studied. The brightest detections were discovered prior to the launches of Kepler and Convection Rotation and planetary Transits (CoRoT; Baglin et al. 2006). This means that most bright stars only have asteroseismology from ground-based radial velocity (RV) measurements, which suffer from aliasing problems due to gaps in data. Examples of well-known ground-based asteroseismic detections include β Hyi (Bedding et al. 2001; Carrier et al. 2001; Bedding et al. 2006), α Cen A (Bouchy & Carrier 2002; Bedding et al. 2004), and α Cen B (Carrier & Bourban 2003; Kjeldsen et al. 2005).
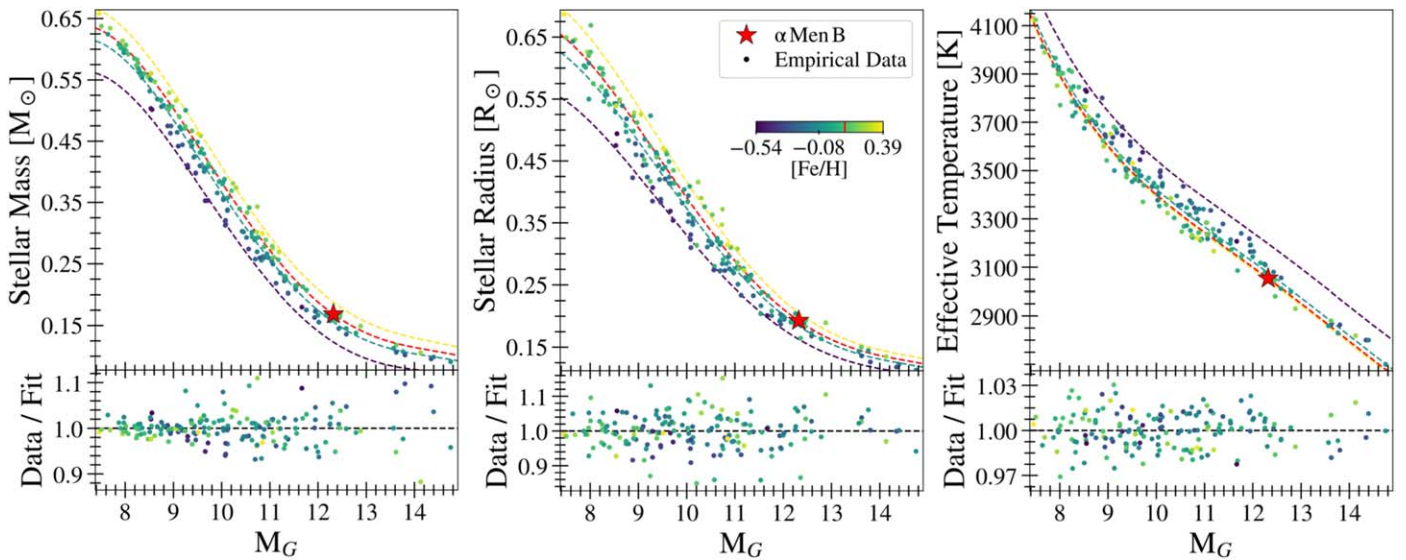
Figure 7. Empirical best-fit relations for mass (left), radius (middle), and temperature (right) as a function of absolute Gaia magnitude for the sample in Mann et al. (2015), color-coded by metallicity. The bottom plots show the residuals of the data subtracted by the best-fit polynomial (black dashed line). The red star represents the location of α Men B.

The flood of continuous high-precision, high-cadence photometry from CoRoT and Kepler marked the start of the so-called "space-based photometry revolution." Kepler revolutionized the field of asteroseismology by detecting oscillations in $\sim$500 main-sequence and subgiant stars. However, most Kepler targets are faint and distant and thus do not have information from complementary techniques such as interferometry. This limitation was only partially solved by novel techniques called "halo" and "smear" photometry, which allowed the production of high-precision light curves for even heavily saturated Kepler stars (Pope et al. 2016; White et al. 2017; Pope et al. 2019a, 2019b).

The TESS mission provides an ideal solution to this problem. Several early asteroseismic detections by TESS were made for bright nearby stars such as ν Ind (Chaplin et al. 2020), HD 38529 (Ball et al. 2020), λ^2 For (Nielsen et al. 2020), 94 Aqr A (Metcalfe et al. 2020), and the first new TESS asteroseismic host, TOI-197 (Huber et al. 2019). Alpha Men A is now the closest solar analog with an asteroseismic detection from space, making it a prime example of a bright benchmark system from the nominal TESS mission. In fact, α Men A was included in Bruntt et al. (2010) but was the only star in the sample without an asteroseismic detection.

5.2. Stellar Activity

The connection between oscillations and activity cycles is important for understanding the long-term magnetic evolution of stars. For example, observations in the Sun have shown a strong correlation between oscillation frequencies and amplitudes with the solar activity cycle (Broomhall et al. 2011). Currently, there are only a handful of examples that exist for stars other than the Sun (e.g., García et al. 2010); therefore, expanding this sample to more stars would be very valuable. Fortunately, TESS is already well positioned for this, as demonstrated by Metcalfe et al. (2020), who combined TESS asteroseismology with 35 yr of activity measurements to study the evolution of rotation and magnetic activity in 94 Aqr Aa.

Stellar activity is traditionally observed indirectly through long-term monitoring of chromospheric emission in the Ca II H

and K lines (Noyes et al. 1984; Baliunas et al. 1995; Henry et al. 1996). More recently, Santos et al. (2010) and Lovis et al. (2011) used RVs derived from the cross-correlation function (CCF) method to show that stellar activity also correlates with parameters from the CCF, like the FWHM and the bisector inverse slope (BIS). Indeed, a study by Zechmeister et al. (2013) compared archival HARPS RVs with three different indicators for $\sim$30 well-studied stars and found a positive correlation with all three ($\log R'_{HK}$, BIS, and FWHM) for α Men, indicative of a magnetic cycle as a cause of the RV variations. However, the main goal of the study was to observationally confirm the existence of correlations in RV indicators, and they did not report any activity cycle periods.

To investigate the stellar activity cycle for α Men A, we collected publicly available RV data from two instruments on the ESO 3.6 m telescope: the Coudé Echelle Spectrograph (CES; pre- and postupgrade) and HARPS, which was already corrected for systemic instrumental offsets in Zechmeister et al. (2013). We also collected data from the Anglo-Australian Planet Search (AAPS), which perfectly overlapped with the CES and HARPS data. Figure 9 shows the complete RV time series, which covers 22 yr. The AAPS data after 2011 are plotted as a separate instrument because of an unexplained RV offset. We used a conservative bin size of 60 days to average over the scatter due to stellar rotation, revealing a period that is similar to that observed in the Sun. Using the publicly available GLS code (Zechmeister & Kürster 2009), a generalized Lomb–Scargle periodogram analysis that is better suited for unevenly (and sparsely) sampled data, we detect a period $P = 13.1 \pm 1.1$ yr in the RV time series. There is evidence for a long-term linear trend that is likely from the companion, depending on the inclination of the system. Note that we did not correct for any additional systematic offsets when we combined the time series from multiple instruments.

To confirm that the RV variations are due to an activity cycle, we analyzed the Mount Wilson calibrated S-index time series available from the HARPS DRS pipeline. Chromospheric emission in α Men was also observed as part of the

Table 5
Secondary Stellar Parameters

Other Identifiers:		
α Men B, HD 43834 B,		
Gaia DR2/eDR3 5264749303457104384		

Parameter	Value	Method
Gaia[a,c]		
RA, α_{J2016}	92.5590	A
decl., δ_{J2016}	−74.7542	A
Parallax, π (mas)	97.8666 ± 0.0898	A
Distance, d (pc)	10.2180 ± 0.0094	A
Gaia G mag, G	12.3653 ± 0.0044	P
Gaia G contrast, ΔG	7.4652 ± 0.0053	P
Other Work[b,d,e]		
Projected separation, ρ_K (arcsec)	3.02 ± 0.01	A
Position angle, PA_K (deg)	250.87 ± 0.11	A
NACO K contrast, Δm_K	4.97 ± 0.05	P
2MASS K_S mag, K_S[f]	8.476 ± 0.200	P
Spectral type	M3.5–M6.5	R1
Stellar mass, $M_\star$ ($M_\odot$)	0.14 ± 0.01	R2
Orbital period, P (yr)	162.04	…
This Work		
Effective temperature, T_{eff} (K)	3054 ± 44	E
Stellar radius, $R_\star$ ($R_\odot$)	0.19 ± 0.01	E
Stellar mass, $M_\star$ ($M_\odot$)	0.169 ± 0.006	E
Age, t (Gyr)	6.2 ± 1.4	F
Orbital period, P (yr)	157.44	…

Notes.
[a] Gaia Collaboration et al. (2016).
[c] Eggenberger et al. (2007).
[d] Cutri et al. (2012).
[b] Gaia Collaboration et al. (2021).
[e] Tokovinin (2014).
[f] The provided K_S magnitude uncertainty for the companion was less than that reported by Cutri et al. (2012) for the primary. Therefore, we inflated the uncertainty in the K_S magnitude for HD 43834 B to reflect that.
Methods: (A) astrometry, (E) empirical relations derived from Mann et al. (2015, 2019), (R1) relationship between absolute magnitude and spectral type from Eggenberger et al. (2007; using data from Delfosse et al. 2000, Leggett et al. 2001, Dahn et al. 2002, and Vrba et al. 2004), (R2) infrared mass–luminosity relation for low-mass stars (Delfosse et al. 2000), (P) photometry, (F) frequency modeling via asteroseismology.

SMARTS southern HK project from 2007 to 2013 (Metcalfe et al. 2009b). The bottom panel of Figure 9 shows the combined S-index time series, which span roughly one activity cycle and follow a similar trend to that seen in the RVs. This suggests that the observed RV variations are intrinsic to the star and not from a long-period planetary mass companion, providing additional evidence in support of an activity cycle detection.

5.3. Gyrochronology

Recent observations of stellar rotation periods have challenged commonly adopted age–rotation relationships in two distinct parameter spaces. Specifically, the observation of slow rotation periods in middle-aged solar-type stars has been proposed to be related to weakened magnetic braking due to stellar winds (van Saders et al. 2016), while the stalled spin-down observed in lower-mass cluster members (Curtis et al. 2019) has been hypothesized to be related to reduced angular momentum transport caused by a decoupling of the convective core and the radiative envelope (Spada & Lanzafame 2020). At an age of ∼6 Gyr, α Men A is in the latter half of its main-sequence life and therefore provides a valuable test for the weakened braking hypothesis. Alpha Men B, on the other hand, is a fully convective M dwarf and thus provides an excellent test of whether core–envelope decoupling is indeed responsible for the stalled spin-down in M dwarfs with radiative envelopes. Consequently, rotation periods for either star in the α Mensae system would be extremely valuable to calibrate gyrochronology, which is currently the most promising method for ages for field dwarfs.

Saar & Osten (1997) reported a rotation period (P_{rot}) of 32 days for α Men based on Ca II flux measurements. Further investigation showed that the rotation period was not directly observed but empirically derived. A relationship between chromospheric activity and the Rossby number (Ro) of a star, a parameterization of the rotation period and convective turnover time (τ_{conv}), was established by Noyes et al. (1984) and updated by Mamajek & Hillenbrand (2008) using a larger sample of stars. For α Men A, a mean activity level $\log R'_{HK} = -4.94$ from Henry et al. (1996) with Equation (5) of Mamajek & Hillenbrand (2008) yields Ro = 2.05. Using Equation (4) from Noyes et al. (1984) and the Johnson color index $(B - V)_J = 0.72$ for the primary, we estimate a turnover time of $\log \tau_c = 1.192$. We arrive at an approximate value of $P_{rot} \sim 32$ days, in agreement with the value reported by Saar & Osten (1997).

We also calculated the color index from the Tycho-2 catalog (Høg et al. 2000) using the transformation from B_T and V_T to Johnson indices (see Section 1.3, Appendix 4 from the Hipparcos catalog; ESA 1997). We used this color index $(B - V)_J = 0.69$ to obtain $\log \tau_c = 1.16$ and $P_{rot} \sim 30$ days. It is also worth pointing out that the updated empirical age–activity–rotation relation from Mamajek & Hillenbrand (2008) estimated an age of 5.5 Gyr for α Men, which is consistent with our asteroseismic age.

To search for stellar rotational modulation, we analyzed the TESS SAP light curve, which is more conservative in preserving long-term variability than the PDCSAP light curve shown in Figure 1. We identified a period of around 36 days, consistent with the estimates from activity indicators. We caution, however, that this period is highly uncertain due to intrasector TESS systematics, which are nonnegligible and therefore make it difficult to detect reliable rotation periods ≳13 days.

Using the asteroseismic age, we calculated the rotation periods of α Men A using different spin-down models. Figure 10 shows the rotation period for the primary as a function of age using Yale Rotating stellar Evolution Code (YREC; Demarque et al. 2008) models with a standard braking law (van Saders & Pinsonneault 2013) and a stalled braking law (van Saders et al. 2016), as implemented in `kiauhoku` (Claytor et al. 2020). The models predict rotation periods of 30.4 ± 4.5 and 29.6 ± 3.0 days, respectively, indicating that α Men A may be close to the critical Rossby number, which is suggested to mark a transition in its rotational behavior (Metcalfe et al. 2016), leading to a weakened spin-down (van Saders et al. 2016).
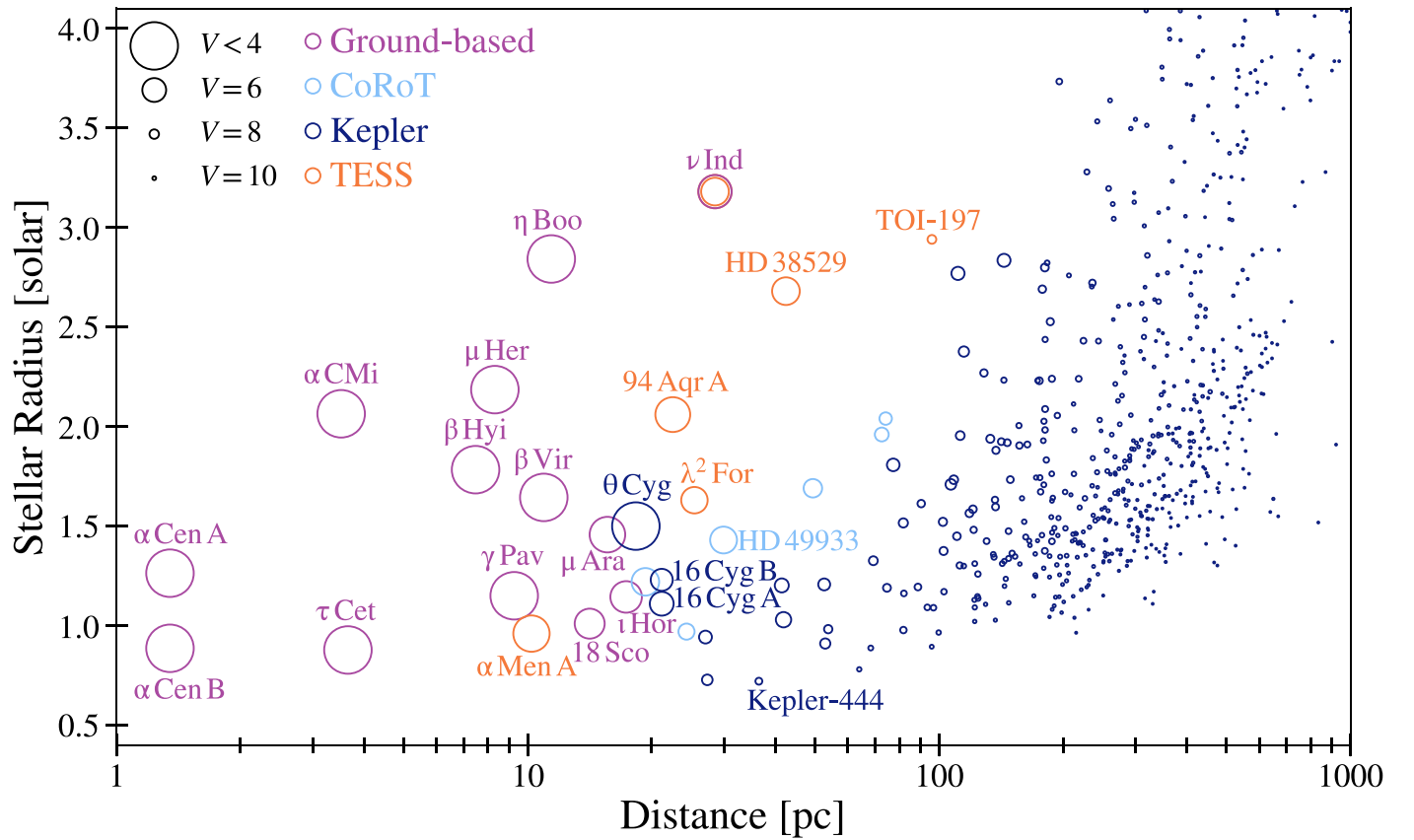
Figure 8. Current population of asteroseismic detections with confirmed $\Delta\nu$ measurements plotted as the stellar size (in solar radii) as a function of distance, where markers are sized by their visual magnitude. Ground-based seismic detections (purple) are limited to close, bright stars, while Kepler (navy blue) found hundreds of oscillations in faint, distant stars. TESS (orange) is beginning to close the gap between these two regimes and hence providing bright nearby targets to follow up with ground-based instruments. In fact, ν Ind is the first example where an early ground-based asteroseismic detection (Bedding et al. 2006) was redetected later with TESS (Chaplin et al. 2020). Label references (in order of proximity): α Cen A (Brown et al. 1991; Bouchy & Carrier 2001, 2002; Butler et al. 2004; Bedding et al. 2004), α Cen B (Carrier & Bourban 2003; Kjeldsen et al. 2005), α CMi (Mosser et al. 1998; Martić et al. 1999; Arentoft et al. 2008; Bedding et al. 2010), τ Cet (Teixeira et al. 2009), β Hyi (Bedding et al. 2001; Carrier et al. 2001; Bedding et al. 2006), μ Her (Bonanno et al. 2008; Grundahl et al. 2017), γ Pav (Mosser et al. 2008), α Men A (this work), β Vir (Carrier et al. 2005b), η Boo (Kjeldsen & Bedding 1995; Kjeldsen et al. 2003; Carrier et al. 2005a), 18 Sco (Bazot et al. 2011), μ Ara (Bouchy et al. 2005), ι Hor (Vauclair et al. 2008), θ Cyg (Guzik et al. 2011), 16 Cyg A and B (Metcalfe et al. 2012b), 94 Aqr A (Metcalfe et al. 2020), λ^2 For (Nielsen et al. 2020), ν Ind (Bedding et al. 2006; Carrier et al. 2007; Chaplin et al. 2020), HD 49933 (Appourchaux et al. 2008; Benomar et al. 2009), Kepler-444 (Campante et al. 2015), HD 38529 (Ball et al. 2020), and TOI-197 (Huber et al. 2019).

Gyrochronology of M dwarfs remains challenging, mostly because the required constraints (e.g., P_{rot}, ages) are not readily available. In particular, α Men B is below the convective boundary, where braking laws are uncertain. While the rotation period for the M dwarf is currently unknown, measuring a period in combination with the asteroseismic age would be valuable for placing better constraints on gyrochronology models in low-mass stars.

5.4. Exoplanet Synergies

The future of exoplanet characterization will be heavily focused on direct imaging, which provides direct information about the planet composition and atmosphere. The next generation of space-based imaging missions (e.g., LUVOIR, The LUVOIR Team 2019; HabEx, Gaudi et al. 2020) will be equipped with instruments capable of imaging Earth-like planets around nearby stars.

A critical challenge for future direct-imaging missions will be target selection. Historically, lower-luminosity M dwarfs have been popular targets when searching for rocky potentially habitable planets, since the habitable zones (HZs) are close to the host star. While this is ideal for methods such as transits and

RVs that yield larger signals for planets that are closer in, the smaller separation is challenging for direct imaging. Consequently, the prime targets for missions like LUVOIR and HabEx will be nearby, well-characterized Sun-like stars whose HZs are further from the host star. Bixel & Apai (2020) discussed the importance of age-based target selection specifically in the context of understanding planet habitability, noting that the presence of oxygen in the Earth's atmosphere has had a rich dynamic history. An Earth analog around α Men A has a predicted separation of $\sim$100 mas and contrast of $\sim 5 \times 10^{-9}$, in reach for next-generation space-based imaging missions.

Additionally, new spectrographs have recently achieved the submeter-per-second precision that is needed to detect an Earth-like planet around a Sun-like star through precise radial velocities (PRVs). A major limitation for these efforts has been the background from stellar signals that have comparable periods and amplitudes to low-mass planetary companions, which can lead to spurious detections. Several newer techniques have been developed to help mitigate the effects induced on PRVs as a result of stellar activity (e.g., Damasso & Del Sordo 2017; Feng et al. 2017; Dumusque 2018;
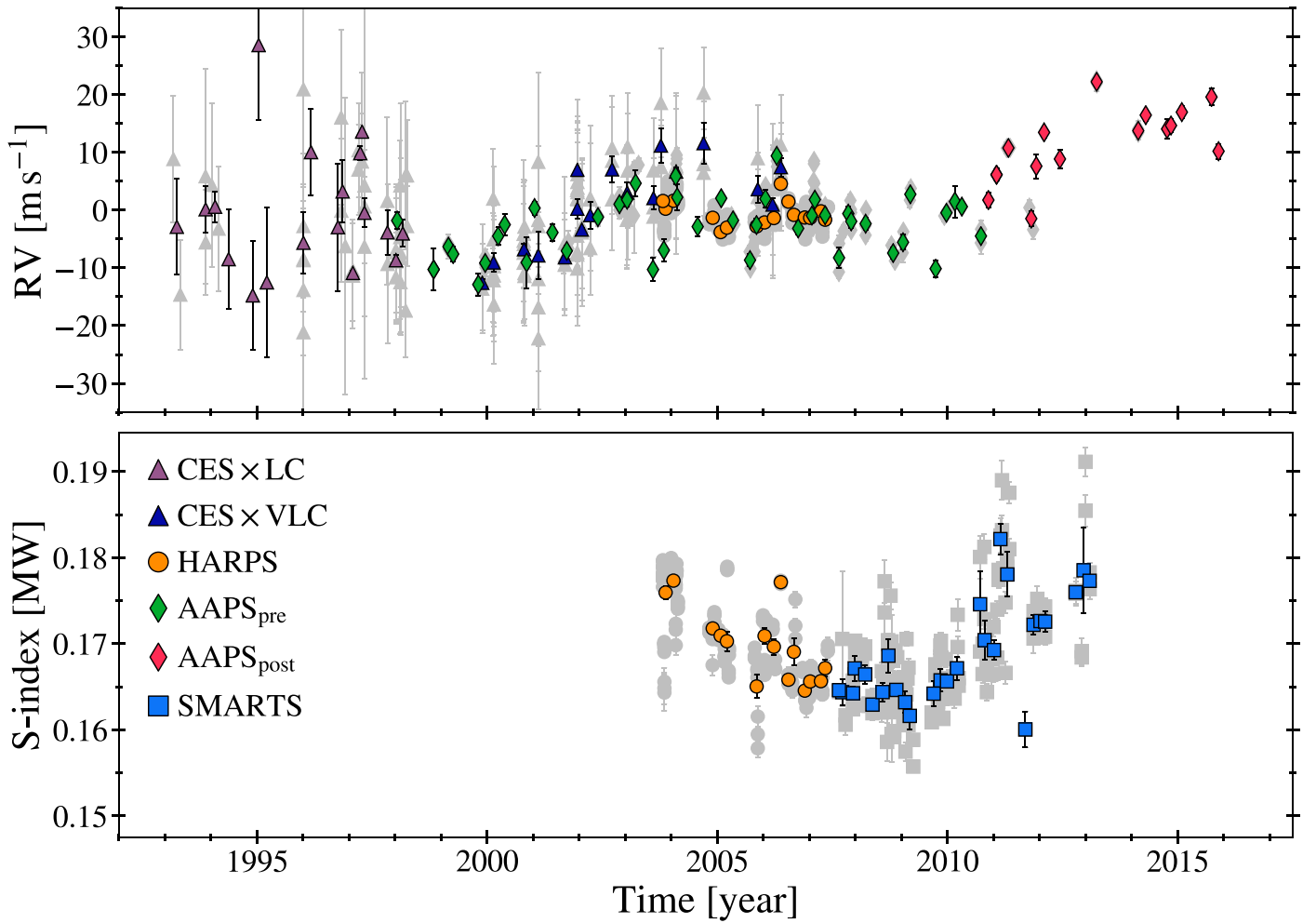
Figure 9. Long-term ground-based RV (top) and Mount Wilson calibrated *S*-index (bottom) time series for α Men A using combined data from five different surveys. Each instrument is shown with a different symbol, where offsets and/or upgrades of a similar instrument are shown with a different color. Gray points are the original data from each survey, and colored points are binned over 60 days. We find a long-term cyclic trend of ∼13 yr in both RVs and chromospheric emission, indicative of a stellar activity cycle.

Zhao & Tinney 2020). Our newly reported activity cycle for α Men A ($P = 13.1 +/- 1.1$ yr with an amplitude of ~5.5 m s^{-1}) is consistent with the long-term RV scatter found in Wittenmyer et al. (2016) and could potentially help disentangle smaller planet-like signals with ground-based PRV surveys.

6. Conclusions

We have used asteroseismology to precisely characterize the solar analog α Men A and its M dwarf companion. Our main conclusions can be summarized as follows.

1. Alpha Men A is a naked-eye G7 dwarf in TESS's SCVZ. Combined astrometric, spectroscopic, and asteroseismic modeling confirmed the solar analog nature, with $R_\star = 0.960 \pm 0.016$ $R_\odot$, $M_\star = 0.961 \pm 0.045$ $M_\odot$, and an age of 6.1 ± 1.4 Gyr. Alpha Men A is the closest star cooler than the Sun with an asteroseismic detection from space-based photometry and demonstrates the power of TESS for cool dwarf asteroseismology.

2. Alpha Men A has a bound companion, which was previously characterized as a mid-to-late M dwarf using 2MASS photometry. Using Gaia eDR3 photometry, we derived empirical M dwarf relations for mass, effective temperature, and radius as a function of metallicity. Using the relations, we provide revised properties of the fully convective late M dwarf ($R_\star = 0.19 \pm 0.01$ $R_\odot$, $M_\star = 0.169 \pm 0.006$ $M_\odot$, $T_{\rm eff} = 3054 \pm 44$ K). Through the asteroseismic characterization of the primary, α Men B joins a very small population of M dwarfs with a precisely measured age.

3. We used a combination of multiple RV surveys to measure an activity cycle of $P = 13.1 \pm 1.1$ yr in α Men A, making it a prime target to investigate the interplay of long-term magnetic evolution and stellar oscillations in a solar-type star.

4. Using the asteroseismic age, we used gyrochronology models to estimate rotation periods of 30.4 ± 4.5 and 29.6 ± 3.0 days using standard and weakened braking laws, respectively. Asteroseismic ages in two low-mass main-sequence stars make the α Mensae system a benchmark calibrator for gyrochronology relations, which is currently the most promising age-dating method for late-type stars.

With a precisely measured age and activity cycle, α Men A is now one of the best-characterized nearby solar analogs, a useful calibrator for stellar astrophysics, and a prime target for next-generation direct-imaging missions to search for
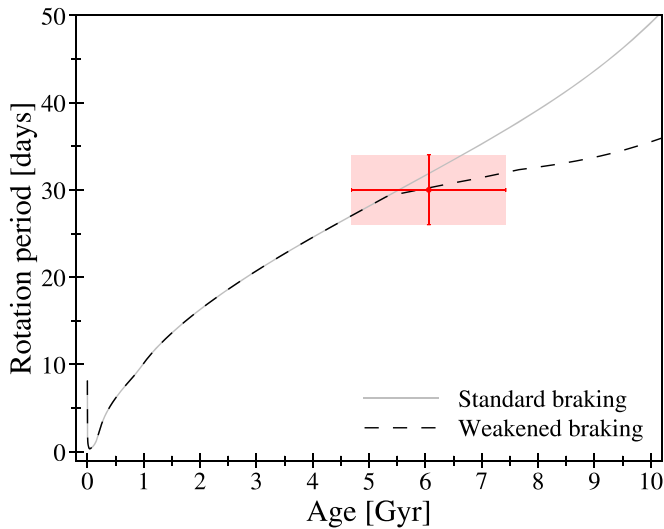
Figure 10. Predicted rotation periods of α Men A from gyrochronology models using a standard braking law (solid gray line; van Saders & Pinsonneault 2013) and a weakened braking law (dashed black line; van Saders et al. 2016). The rotation period uncertainties were calculated by taking the average of the lower and upper quantiles from the corner plots derived by kiauhoku (Claytor et al. 2020), where the more conservative uncertainty of 4.5 days is plotted in this figure. The shaded red area represents the 1σ uncertainty region for the location of α Men A with respect to theoretical gyrochronological models, which predict that the solar analog has recently undergone or is currently in transition in its rotational behavior.

Earth-like planets. Continued all-sky TESS observations, in particular using 20 s cadence observations started in the extended mission, will enable asteroseismic detections in other solar analogs and continue the powerful synergies between stellar astrophysics and exoplanet science enabled by space-based photometry.

ORCID iDs

Ashley Chontos ⊙ https://orcid.org/0000-0003-1125-2564
Daniel Huber ⊙ https://orcid.org/0000-0001-8832-4488
Travis A. Berger ⊙ https://orcid.org/0000-0002-2580-3614
Aldo M. Serenelli ⊙ https://orcid.org/0000-0001-6359-2769
Victor Silva Aguirre ⊙ https://orcid.org/0000-0002-6137-903X
Warrick H. Ball ⊙ https://orcid.org/0000-0002-4773-1017
Sarbani Basu ⊙ https://orcid.org/0000-0002-6163-3472
Timothy R. Bedding ⊙ https://orcid.org/0000-0001-5222-4661
William J. Chaplin ⊙ https://orcid.org/0000-0002-5714-8618
Zachary R. Claytor ⊙ https://orcid.org/0000-0002-9879-3904
Enrico Corsaro ⊙ https://orcid.org/0000-0001-8835-2075
Rafael A. Garcia ⊙ https://orcid.org/0000-0002-8854-3776
Steve B. Howell ⊙ https://orcid.org/0000-0002-2532-2853
Mia S. Lundkvist ⊙ https://orcid.org/0000-0002-8661-2571
Savita Mathur ⊙ https://orcid.org/0000-0002-0129-0316
Travis S. Metcalfe ⊙ https://orcid.org/0000-0003-4034-0416
Martin B. Nielsen ⊙ https://orcid.org/0000-0001-9169-2599
Jia Mian Joel Ong ⊙ https://orcid.org/0000-0001-7664-648X
Maissa Salama ⊙ https://orcid.org/0000-0002-5082-6332
Keivan G. Stassun ⊙ https://orcid.org/0000-0002-3481-9052
R. H. D. Townsend ⊙ https://orcid.org/0000-0002-2522-8605
Jennifer L. van Saders ⊙ https://orcid.org/0000-0002-4284-8638

Mutlu Yildiz ⬤ https://orcid.org/0000-0002-7772-7641
R. Paul Butler ⬤ https://orcid.org/0000-0003-1305-3761
C. G. Tinney ⬤ https://orcid.org/0000-0002-7595-0970
Robert A. Wittenmyer ⬤ https://orcid.org/0000-0001-9957-9304

References

Appourchaux, T., Michel, E., Auvergne, M., et al. 2008, A&A, 488, 705
Arentoft, T., Kjeldsen, H., Bedding, T. R., et al. 2008, ApJ, 687, 1180
Astropy Collaboration, Robitaille, T. P., & Tollerud, E. J. 2013, A&A, 558, A33
Baglin, A., Auvergne, M., Boisnard, L., et al. 2006, in 36th COSPAR Scientific Assembly, Vol. 36 (Paris: ESA), 3749
Baliunas, S. L., Donahue, R. A., Soon, W. H., et al. 1995, ApJ, 438, 269
Ball, W. H., Chaplin, W. J., Nielsen, M. B., et al. 2020, MNRAS, 499, 6084
Ball, W. H., & Gizon, L. 2014, A&A, 568, A123
Barnes, S. A. 2007, ApJ, 669, 1167
Basu, S., Chaplin, W. J., & Elsworth, Y. 2010, ApJ, 710, 1596
Basu, S., Verner, G. A., Chaplin, W. J., & Elsworth, Y. 2012, ApJ, 746, 76
Bazot, M., Ireland, M. J., Huber, D., et al. 2011, A&A, 526, L4
Bedding, T. R., Butler, R. P., Carrier, F., et al. 2006, ApJ, 647, 558
Bedding, T. R., Butler, R. P., Kjeldsen, H., et al. 2001, ApJL, 549, L105
Bedding, T. R., Kjeldsen, H., Butler, R. P., et al. 2004, ApJ, 614, 380
Bedding, T. R., Kjeldsen, H., Campante, T. L., et al. 2010, ApJ, 713, 935
Benomar, O., Baudin, F., Campante, T. L., et al. 2009, A&A, 507, L13
Bensby, T., Feltzing, S., & Lundström, I. 2003, A&A, 410, 527
Bensby, T., Feltzing, S., & Oey, M. S. 2014, A&A, 562, A71
Berger, T. A., Huber, D., van Saders, J. L., et al. 2020, AJ, 159, 280
Bixel, A., & Apai, D. 2020, ApJ, 896, 131
Bonanno, A., Benatti, S., Claudi, R., et al. 2008, ApJ, 676, 1248
Bond, J. C., Tinney, C. G., Butler, R. P., et al. 2006, MNRAS, 370, 163
Borucki, W. J., Koch, D., Basri, G., et al. 2010, Sci, 327, 977
Bouchy, F., Bazot, M., Santos, N. C., Vauclair, S., & Sosnowska, D. 2005, A&A, 440, 609
Bouchy, F., & Carrier, F. 2001, A&A, 374, L5
Bouchy, F., & Carrier, F. 2002, A&A, 390, 205
Bovy, J., Rix, H.-W., Green, G. M., Schlafly, E. F., & Finkbeiner, D. P. 2016, ApJ, 818, 130
Broomhall, A. M., Chaplin, W. J., Elsworth, Y., & New, R. 2011, MNRAS, 413, 2978
Brown, T. M., Gilliland, R. L., Noyes, R. W., & Ramsey, L. W. 1991, ApJ, 368, 599
Bruntt, H., Bedding, T. R., Quirion, P. O., et al. 2010, MNRAS, 405, 1907
Butler, R. P., Bedding, T. R., Kjeldsen, H., et al. 2004, ApJL, 600, L75
Campante, T. L., Barclay, T., Swift, J. J., et al. 2015, ApJ, 799, 170
Carrier, F., Bouchy, F., Kienzle, F., et al. 2001, A&A, 378, 142
Carrier, F., & Bourban, G. 2003, A&A, 406, L23
Carrier, F., Eggenberger, P., & Bouchy, F. 2005a, A&A, 434, 1085
Carrier, F., Eggenberger, P., D'Alessandro, A., & Weber, L. 2005b, NewA, 10, 315
Carrier, F., Kjeldsen, H., Bedding, T. R., et al. 2007, A&A, 470, 1059
Casagrande, L., Schönrich, R., Asplund, M., et al. 2011, A&A, 530, A138
Chaplin, W. J., Basu, S., Huber, D., et al. 2014, ApJS, 210, 1
Chaplin, W. J., Serenelli, A. M., Miglio, A., et al. 2020, NatAs, 4, 382
Choi, J., Dotter, A., Conroy, C., et al. 2016, ApJ, 823, 102
Chontos, A., Huber, D., Latham, D. W., et al. 2019, AJ, 157, 192
Christensen-Dalsgaard, J. 2008, Ap&SS, 316, 13
Claytor, Z. R., van Saders, J. L., Santos, Â. R. G., et al. 2020, ApJ, 888, 43
Corsaro, E., & De Ridder, J. 2014, A&A, 571, A71
Corsaro, E., De Ridder, J., & García, R. A. 2018, A&A, 612, C2
Corsaro, E., Mathur, S., García, R. A., et al. 2017, A&A, 605, A3
Curtis, J. L., Agüeros, M. A., Douglas, S. T., & Meibom, S. 2019, ApJ, 879, 49
Cutri, R. M., Skrutskie, M. F., van Dyk, S., et al. 2003, The IRSA 2MASS All-Sky Point Source Catalog (Washington, DC: NASA)
Cutri, R. M., Skrutskie, M. F., van Dyk, S., et al. 2012, VizieR Online Data Catalog, II/281
da Silva, R., Porto de Mello, G. F., Milone, A. C., et al. 2012, A&A, 542, A84
Dahn, C. C., Harris, H. C., Vrba, F. J., et al. 2002, AJ, 124, 1170
Damasso, M., & Del Sordo, F. 2017, A&A, 599, A126
Delfosse, X., Forveille, T., Ségransan, D., et al. 2000, A&A, 364, 217
Demarque, P., Guenther, D. B., Li, L. H., Mazumdar, A., & Straka, C. W. 2008, Ap&SS, 316, 31
Demarque, P., Woo, J.-H., Kim, Y.-C., & Yi, S. K. 2004, ApJS, 155, 667
Dotter, A., Chaboyer, B., Jevremović, D., et al. 2007, AJ, 134, 376

Dotter, A., Chaboyer, B., Jevremović, D., et al. 2008, ApJS, 178, 89
Douglas, S. T., Curtis, J. L., Agüeros, M. A., et al. 2019, ApJ, 879, 100
Dumusque, X. 2018, A&A, 620, A47
Eggenberger, A., Udry, S., Chauvin, G., et al. 2007, A&A, 474, 273
Eiroa, C., Marshall, J. P., Mora, A., et al. 2013, A&A, 555, A11
Evans, D. W., Riello, M., De Angeli, F., et al. 2018, A&A, 616, A4
Feng, F., Tuomi, M., & Jones, H. R. A. 2017, MNRAS, 470, 4794
Foreman-Mackey, D., Hogg, D. W., Lang, D., & Goodman, J. 2013, PASP, 125, 306
Gai, N., Basu, S., Chaplin, W. J., & Elsworth, Y. 2011, ApJ, 730, 63
Gaia Collaboration, Brown, A. G. A., Vallenari, A., et al. 2018, A&A, 616, A1
Gaia Collaboration, Brown, A. G. A., Vallenari, A., et al. 2021, A&A, 649, A1
Gaia Collaboration, Prusti, T., de Bruijne, J. H. J., et al. 2016, A&A, 595, A1
García, R. A., & Ballot, J. 2019, LRSP, 16, 4
García, R. A., Mathur, S., Salabert, D., et al. 2010, Sci, 329, 1032
García, R. A., Régulo, C., Samadi, R., et al. 2009, A&A, 506, 41
GarcÍa, R. A., Régulo, C., Turck-Chièze, S., et al. 2001, SoPh, 200, 361
Gaudi, B. S., Seager, S., Mennesson, B., et al. 2020, arXiv:2001.06683
Girardi, L., Bressan, A., Bertelli, G., & Chiosi, C. 2000, A&AS, 141, 371
Gray, R. O., Corbally, C. J., Garrison, R. F., et al. 2006, AJ, 132, 161
Grevesse, N., & Noels, A. 1993, PhST, 47, 133
Grundahl, F., Fredslund Andersen, M., Christensen-Dalsgaard, J., et al. 2017, ApJ, 836, 142
Guzik, J. A., Houdek, G., Chaplin, W. J., et al. 2011, arXiv:1110.2120
Handberg, R., & Campante, T. L. 2011, A&A, 527, A56
Harvey, J. 1985, in ESA Special Publication, Vol. 235, Future Missions in Solar, Heliospheric & Space Plasma Physics, ed. E. Rolfe & B. Battrick (Noordwijk: ESA), 199
Hawkins, K., Jofré, P., Heiter, U., et al. 2016, A&A, 592, A70
Heller, R., Hippke, M., & Kervella, P. 2017, AJ, 154, 115
Henry, T. J., Soderblom, D. R., Donahue, R. A., & Baliunas, S. L. 1996, AJ, 111, 439
Hey, D., & Ball, W. 2020, Echelle: Dynamic echelle diagrams forasteroseismology v1.4, Zenodo, doi:10.5281/zenodo.3629933
Høg, E., Fabricius, C., Makarov, V. V., et al. 2000, A&A, 355, L27
Howell, S. B., Everett, M. E., Sherry, W., Horch, E., & Ciardi, D. R. 2011, AJ, 142, 19
Huber, D. 2017, Isoclassify: v1.2, Zenodo, doi:10.5281/zenodo.573372
Huber, D., Chaplin, W. J., Chontos, A., et al. 2019, AJ, 157, 245
Huber, D., Stello, D., Bedding, T. R., et al. 2009, CoAst, 160, 74
Jenkins, J. M., Twicken, J. D., McCauliff, S., et al. 2016, Proc. SPIE, 9913, 99133E
Kjeldsen, H., & Bedding, T. R. 1995, A&A, 293, 87
Kjeldsen, H., Bedding, T. R., Baldry, I. K., et al. 2003, AJ, 126, 1483
Kjeldsen, H., Bedding, T. R., Butler, R. P., et al. 2005, ApJ, 635, 1281
Kjeldsen, H., Bedding, T. R., & Christensen-Dalsgaard, J. 2008, ApJL, 683, L175
Kraft, R. P. 1967, ApJ, 150, 551
Leggett, S. K., Allard, F., Geballe, T. R., Hauschildt, P. H., & Schweitzer, A. 2001, ApJ, 548, 908
Lindegren, L., Klioner, S. A., Hernández, J., et al. 2021, A&A, 649, A2
Lomb, N. R. 1976, Ap&SS, 39, 447
Lovis, C., Dumusque, X., Santos, N. C., et al. 2011, arXiv:1107.5325
Luck, R. E. 2018, AJ, 155, 111
Lundkvist, M. S., Kjeldsen, H., & Silva Aguirre, V. 2014, A&A, 566, 82
Maldonado, J., Eiroa, C., Villaver, E., Montesinos, B., & Mora, A. 2012, A&A, 541, A40
Maldonado, J., Eiroa, C., Villaver, E., Montesinos, B., & Mora, A. 2015, A&A, 579, A20
Mamajek, E. E., & Hillenbrand, L. A. 2008, ApJ, 687, 1264
Mann, A. W., Dupuy, T., Kraus, A. L., et al. 2019, ApJ, 871, 63
Mann, A. W., Feiden, G. A., Gaidos, E., Boyajian, T., & von Braun, K. 2015, ApJ, 804, 64
Marigo, P., Girardi, L., Bressan, A., et al. 2008, A&A, 482, 883
Marques, J. P., Goupil, M. J., Lebreton, Y., et al. 2013, A&A, 549, A74
Martić, M., Schmitt, J., Lebrun, J. C., et al. 1999, A&A, 351, 993
Mathur, S., García, R. A., Régulo, C., et al. 2010, A&A, 511, A46
Mathur, S., Hekker, S., Trampedach, R., et al. 2011, ApJ, 741, 119
McDonald, I., Zijlstra, A. A., & Watson, R. A. 2017, MNRAS, 471, 770
McQuillan, A., Mazeh, T., & Aigrain, S. 2014, ApJS, 211, 24
Mermilliod, J. C. 2006, VizieR Online Data Catalog, II/168
Metcalfe, T. S., Chaplin, W. J., Appourchaux, T., et al. 2012b, ApJL, 748, L10
Metcalfe, T. S., & Charbonneau, P. 2003, JCoPh, 185, 176
Metcalfe, T. S., Creevey, O. L., & Christensen-Dalsgaard, J. 2009a, ApJ, 699, 373
Metcalfe, T. S., Egeland, R., & van Saders, J. 2016, ApJL, 826, L2

Metcalfe, T. S., Judge, P. G., Basu, S., et al. 2009b, arXiv:0909.5464
Metcalfe, T. S., Mathur, S., & Doğan, G. 2012a, in ASP Conf. Ser. 462, Progress in Solar/Stellar Physics with Helio- and Asteroseismology, ed. H. Shibahashi, M. Takata, & A. E. Lynas-Gray (San Francisco, CA: ASP), 213
Metcalfe, T. S., van Saders, J. L., Basu, S., et al. 2020, ApJ, 900, 154
Mier, P. R. 2017, Pablormier/Yabox: V1.0.3, v1.0.3, Zenodo, doi:10.5281/zenodo.848679
Morel, P., & Lebreton, Y. 2008, Ap&SS, 316, 61
Mosser, B., Deheuvels, S., Michel, E., et al. 2008, A&A, 488, 635
Mosser, B., Maillard, J. P., Mekarnia, D., & Gay, J. 1998, A&A, 340, 457
Nielsen, M. B., Ball, W. H., Standing, M. R., et al. 2020, A&A, 641, A25
Nielsen, M. B., Gizon, L., Schunker, H., & Karoff, C. 2013, A&A, 557, L10
Nielsen, M. B., Schunker, H., Gizon, L., & Ball, W. H. 2015, A&A, 582, A10
Nielsen, M. B., Schunker, H., Gizon, L., Schou, J., & Ball, W. H. 2017, A&A, 603, A6
Noyes, R. W., Hartmann, L. W., Baliunas, S. L., Duncan, D. K., & Vaughan, A. H. 1984, ApJ, 279, 763
Paunzen, E. 2015, A&A, 580, A23
Paxton, B., Bildsten, L., Dotter, A., et al. 2011, ApJS, 192, 3
Paxton, B., Cantiello, M., Arras, P., et al. 2013, ApJS, 208, 4
Paxton, B., Marchant, P., Schwab, J., et al. 2015, ApJS, 220, 15
Paxton, B., Schwab, J., Bauer, E. B., et al. 2018, ApJS, 234, 34
Paxton, B., Smolec, R., Schwab, J., et al. 2019, ApJS, 243, 10
Pietrinferni, A., Cassisi, S., Salaris, M., & Castelli, F. 2004, ApJ, 612, 168
Pope, B. J. S., Davies, G. R., Hawkins, K., et al. 2019a, ApJS, 244, 18
Pope, B. J. S., White, T. R., Huber, D., et al. 2016, MNRAS, 455, L36
Pope, B. J. S., White, T. R., Farr, W. M., et al. 2019b, ApJS, 245, 8
Ramírez, I., Allende Prieto, C., & Lambert, D. L. 2007, A&A, 465, 271
Ramírez, I., Fish, J. R., Lambert, D. L., & Allende Prieto, C. 2012, ApJ, 756, 46
Reinhold, T., Reiners, A., & Basri, G. 2013, A&A, 560, A4
Ricker, G. R., Winn, J. N., Vanderspek, R., et al. 2015, JATIS, 1, 014003
Riello, M., De Angeli, F., Evans, D. W., et al. 2021, A&A, 649, A3
Saar, S. H., & Osten, R. A. 1997, MNRAS, 284, 803
Santos, A. R. G., García, R. A., Mathur, S., et al. 2019, ApJS, 244, 21
Santos, N. C., Gomes da Silva, J., Lovis, C., & Melo, C. 2010, A&A, 511, A54
Santos, N. C., Israelian, G., & Mayor, M. 2001, A&A, 373, 1019
Santos, N. C., Israelian, G., & Mayor, M. 2004, A&A, 415, 1153
Scargle, J. D. 1982, ApJ, 263, 835
Schofield, M., Chaplin, W. J., Huber, D., et al. 2019, ApJS, 241, 12

Schwarz, G. 1978, AnSta, 6, 461
Serenelli, A., Johnson, J., Huber, D., et al. 2017, ApJS, 233, 23
Serenelli, A. M., Bergemann, M., Ruchti, G., & Casagrande, L. 2013, MNRAS, 429, 3645
Silva Aguirre, V., Basu, S., Brandão, I. M., et al. 2013, ApJ, 769, 141
Silva Aguirre, V., Casagrande, L., Basu, S., et al. 2012, ApJ, 757, 99
Silva Aguirre, V., Davies, G. R., Basu, S., et al. 2015, MNRAS, 452, 2127
Silva Aguirre, V., Lund, M. N., Antia, H. M., et al. 2017, ApJ, 835, 173
Skrutskie, M. F., Cutri, R. M., Stiening, R., et al. 2006, AJ, 131, 1163
Skumanich, A. 1972, ApJ, 171, 565
Soderblom, D. R. 2010, ARA&A, 48, 581
Soderblom, D. R., Duncan, D. K., & Johnson, D. R. H. 1991, ApJ, 375, 722
Spada, F., & Lanzafame, A. C. 2020, A&A, 636, A76
Stassun, K. G., Collins, K. A., & Gaudi, B. S. 2017, AJ, 153, 136
Stassun, K. G., Corsaro, E., Pepper, J. A., & Gaudi, B. S. 2018, AJ, 155, 22
Stassun, K. G., & Torres, G. 2018, ApJ, 862, 61
Stevens, D. J., Stassun, K. G., & Gaudi, B. S. 2017, AJ, 154, 259
Teixeira, T. C., Kjeldsen, H., Bedding, T. R., et al. 2009, A&A, 494, 237
The LUVOIR Team 2019, arXiv:1912.06219
Thoul, A. A., Bahcall, J. N., & Loeb, A. 1994, ApJ, 421, 828
Tokovinin, A. 2014, AJ, 147, 86
Townsend, R. H. D., & Teitler, S. A. 2013, MNRAS, 435, 3406
Valenti, J. A., & Fischer, D. A. 2005, ApJS, 159, 141
van Saders, J. L., Ceillier, T., Metcalfe, T. S., et al. 2016, Natur, 529, 181
van Saders, J. L., & Pinsonneault, M. H. 2013, ApJ, 776, 67
Vauclair, S., Laymand, M., Bouchy, F., et al. 2008, A&A, 482, L5
Vernazza, J. E., Avrett, E. H., & Loeser, R. 1981, ApJS, 45, 635
Vrba, F. J., Henden, A. A., Luginbuhl, C. B., et al. 2004, AJ, 127, 2948
Weiss, A., & Schlattl, H. 2008, Ap&SS, 316, 99
White, T. R., Pope, B. J. S., Antoci, V., et al. 2017, MNRAS, 471, 2882
Wilson, O. C. 1963, ApJ, 138, 832
Wilson, O. C. 1966, ApJ, 144, 695
Wilson, O. C. 1978, ApJ, 226, 379
Wittenmyer, R. A., Butler, R. P., Tinney, C. G., et al. 2016, ApJ, 819, 28
Wright, J. T., Marcy, G. W., Butler, R. P., & Vogt, S. S. 2004, ApJS, 152, 261
Yıldız, M., çelik Orhan, Z., & Kayhan, C. 2019, MNRAS, 489, 1753
Zechmeister, M., & Kürster, M. 2009, A&A, 496, 577
Zechmeister, M., & Kürster, M. 2018, GLS: Generalized Lomb-Scargle periodogram, Astrophysics Source Code Library, ascl:1807.019
Zechmeister, M., Kürster, M., Endl, M., et al. 2013, A&A, 552, A78
Zhao, J., & Tinney, C. G. 2020, MNRAS, 491, 4131